The Astrophysical Journal, 922:51 (9pp), 2021 November 20 https://doi.org/10.3847/1538-4357/ac2900

The Evolution of Collisionless Magnetic Reconnection from Electron Scales to Ion Scales

Dongkuan Liu[1,2], Kai Huang[1,2], Quanming Lu[1,2], San Lu[1,2], Rongsheng Wang[1,2], Weixing Ding[3], and Shui Wang[1,2]
[1] CAS Key Laboratory of Geospace Environment, Department of Geophysics and Planetary Science, University of Science and Technology of China, Hefei, Anhui, People's Republic of China; inhk@ustc.edu.cn, qmlu@ustc.edu.cn
[2] CAS Center for Excellence in Comparative Planetology, People's Republic of China
[3] Department of Plasma Physics and Nuclear Engineering, University of Science and Technology of China, Hefei, Anhui, People's Republic of China
Received 2021 May 27; revised 2021 September 4; accepted 2021 September 20; published 2021 November 19

Abstract

It is generally accepted that collisionless magnetic reconnection is initiated on electron scales, which is mediated by electron kinetics. In this paper, by performing a two-dimensional particle-in-cell simulation, we investigate the transition of collisionless magnetic reconnection from electron scales to ion scales in a Harris current sheet with and without a guide field. The results show that after magnetic reconnection is triggered on electron scales, the electrons are first accelerated by the reconnection electric field around the X line, and then leave away along the outflow direction. In the Harris current sheet without a guide field, the electron outflow is symmetric and directed away from the X line along the center of the current sheet, while the existence of a guide field will distort the symmetry of the electron outflow. In both cases, the high-speed electron outflow is decelerated due to the existence of the magnetic field B_z, then leading to the pileup of B_z. With the increase of B_z, the ions are accelerated by the Lorentz force in the outflow direction, and an ion outflow at about one Alfvén speed is at last formed. In this way, collisionless magnetic reconnection is transferred from the electron scales to the ion scales.

Unified Astronomy Thesaurus concepts: Plasma physics (2089); Planetary magnetospheres (997); Space plasmas (1544); Plasma astrophysics (1261); Solar magnetic reconnection (1504)

1. Introduction

As an important physical process in astrophysical and space plasmas, magnetic reconnection converts the energy stored in the magnetic field into plasma kinetic energy, and it is associated with the topological change of the magnetic field lines (Giovanelli 1946; Parker 1957; Sweet 1958; Vasyliunas 1974; Biskamp 2000; Wang & Lu 2019). Many explosive phenomena in the solar atmosphere, Earth's magnetosphere, and laboratory plasmas are considered to be related to magnetic reconnection (Forbes & Priest 1982; Schindler 1991; Ji et al. 1998; Yamada 1999; Angelopoulos et al. 2008; Birn & Hesse 2009; Pu et al. 2010). However, in general, the reconnection rate predicted by the proposed reconnection models based on magnetohydrodynamical (MHD) theory, like the Sweet–Parker model, is too small to account for these explosive phenomena. Collisionless magnetic reconnection, which relies on particles kinetics, provides a possible solution to this puzzle.

In collisionless magnetic reconnection, the diffusion region, where the magnetic energy is dissipated and the motions between the particles and the magnetic field are decoupled, can be depicted in two characteristic regions: the electron diffusion region (EDR) and the ion diffusion region (IDR). In the IDR, the ions are demagnetized, while the electrons are magnetized and keep drifting toward the vicinity of the X line with a bulk velocity until arriving at the EDR. In the EDR, the electrons are demagnetized from the magnetic field (Hesse et al. 1999; Wang et al. 2000; Pritchett 2001). The electrons are dominantly accelerated by the reconnection electric field in the EDR (Drake et al. 2005; Fu et al. 2006; Liu et al. 2017), while the majority of ions are accelerated in the IDR through the kinetic meandering process and experience Speiser-type effect (Speiser 1965; Pei et al. 2001; Aunai et al. 2011), and eventually both the electrons and ions flow away from the X line in the downstream region. This leads to the formation of the Hall current system and generation of the bipolar Hall electric field together with the quadrupole structure of the out-of-plane magnetic field in the IDR, which have been generally regarded as important signatures of collisionless reconnection (Shay et al. 1998; Bhattacharjee et al. 2001; Pritchett 2001; Karimabadi et al. 2004; Ren et al. 2005; Daughton & Karimabadi 2007; Shay et al. 2007; Lu et al. 2010; Zhou et al. 2015; Huang et al. 2017; Wang et al. 2017; Sang et al. 2019). The above descriptions of collisionless magnetic reconnection assume that reconnection remains in a steady state, and the order of the local reconnection rate is ∼0.1 (Shay et al. 1999; Wan & Lapenta 2008; Liu et al. 2017).

Nevertheless, the magnetic reconnection that occurs in nature is usually in an unsteady state, and it begins from an onset phase. It is generally believed that the prerequisite for the trigger of magnetic reconnection is the formation of a thin current sheet (Hesse & Schindler 2001; Birn & Hesse 2014; Liu et al. 2014), which is then destabilized by the collisionless tearing mode instability (Coppi et al. 1966; Drake & Lee 1977; Lu et al. 2013). Recent kinetic simulations have found that during the onset of reconnection, the current sheet should be at first thinned to an electron scale spontaneously or driven by an external force (Liu et al. 2020; Lu et al. 2020). The thin current sheet is formed due to the pileup of magnetic flux in the upstream, because at this stage the reconnection rate is still too low to convert the upstream magnetic flux to the downstream magnetic flux (Liu et al. 2020). Obviously, the onset phase of reconnection is mediated by electron kinetics. However, magnetic reconnection will at last evolve into ion scales after its onset phase, which has been demonstrated by kinetic simulations (Lu et al. 2020), and one salient feature during this stage is the formation of ion outflow at about one Alfvén speed (e.g., Pritchett 2001; Lu et al. 2010). As we know, the process of magnetic reconnection from electron scales at the onset phase to ion scales has never been reported. In this paper, with a two-dimensional particle-in-cell simulation model, we try to reveal the underlying mechanism for such a transition during collisionless magnetic reconnection.

The outline of the paper is as follows. Section 2 describes the 2D PIC simulation model and initial equilibrium configuration. Section 3 presents the simulation results. Section 4 gives the summary and discussion of the present research.

2. Simulation Model

A 2D PIC simulation model (two spatial dimensions and all three velocity components) is used in this paper to study the evolution of collisionless magnetic reconnection. In this model, the electromagnetic fields are defined on the grids and advanced by solving the Maxwell equations with a full explicit algorithm, and both ions and electrons are advanced in the electromagnetic field by integrating the Newton-Lorentz equations. The developed code based on this model has been successfully performed to study magnetic reconnection (Fu et al. 2006; Lu et al. 2010; Huang et al. 2013; Lu et al. 2013; Liu et al. 2020). In our simulation model, we consider a 1D Harris sheet equilibrium configuration in the (x, z) plane (Harris 1962), and the initial magnetic field is given by

$$\boldsymbol{B}(z) = B_0 \tanh(z/\delta)\boldsymbol{e}_x + B_{y0}\boldsymbol{e}_y. \quad (1)$$

where B_0 is the asymptotical magnetic field, B_{y0} is the initial uniform guide field, δ is the half-width of the current sheet, and the particle number density is given by

$$n(z) = n_b + n_0 \,\mathrm{sech}^2(z/\delta). \quad (2)$$

Here, n_b is the number density of the background plasma, and n_0 is the peak Harris number density. The initial distribution functions for the ions and electrons are Maxwellian with a drift speed in the y direction, the drift speed satisfies the equation $V_{i0}/V_{e0} = -T_{i0}/T_{e0}$, where V_{i0} (V_{e0}) and T_{i0} (T_{e0}) are the initial drift speed and the temperature of ions (electrons).

In our simulations, the size of the simulation domain is $L_x \times L_z = 50d_i \times 50d_i$, where $d_i = c/\omega_{pi}$ is the ion inertial length defined by the peak Harris density n_0. We employ an $N_x \times N_z = 1000 \times 1000$ grid system in our simulation, the grid size is $\Delta x = \Delta z = 0.05d_i$, and the time step is $\Omega_i \Delta t = 0.001$ (where $\Omega_i = eB_0/m_i$ is the ion gyrofrequency based on B_0). In the simulation, the time and velocity are normalized by Ω_{ci}^{-1} and V_A (where $V_A = B_0/\sqrt{\mu_0 n_0 m_i}$ is the Alfvén speed based on B_0 and n_0). We employ more than 10^8 particles per species, and set $T_{i0}/T_{e0} = 4$ ($T_{i0} = 0.4m_iV_A^2$ and $T_{e0} = 0.1m_iV_A^2$) and $n_b = 0.2n_0$. The initial width of the current sheet is $\delta = 0.5d_i$, the ion-to-electron mass ratio is 100, and $c = 15V_A$ (where c is the speed of light). The periodic boundary conditions are employed along the x direction, while the ideal conducting boundary conditions for the electromagnetic fields are employed in the z direction. To study the spontaneous evolution of the magnetic reconnection, we do not employ an initial flux perturbation. The box is long enough in the downstream direction (x) and wide enough in the upstream direction (z), and the influence of the boundary effects can be reduced as much as possible. In this paper, we at first describe the results of the antiparallel reconnection, and then we describe the magnetic reconnection with a uniform guide field $B_{y0} = B_0$.

3. Simulation Results

3.1. Antiparallel Reconnection

Figure 1 plots the time evolution of the reconnection electric field at the X line (E_y) and the half-width of the current sheet (δ)

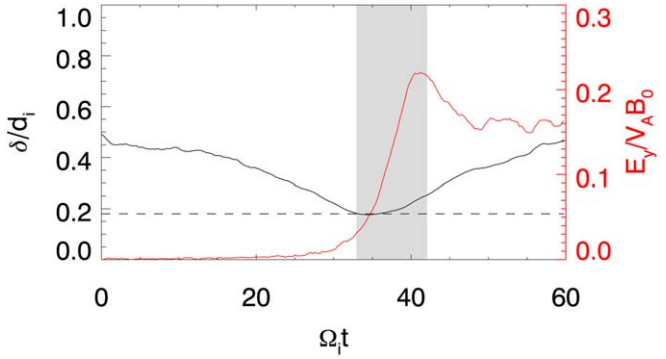

Figure 1. The time evolution of the reconnection electric field E_y at the X line (red line) and the half-thickness of the electron current sheet δ (black line) in the antiparallel reconnection, the dashed line represents the minimum of the δ (about $0.18d_i$, which is equal to $1.8d_e$). We focus on the fast reconnection phase in the gray period from $\Omega_i t = 33$ to $\Omega_i t = 42$.

across the X line in the antiparallel reconnection. Here, the reconnection electric field E_y is obtained by the time derivative of the reconnected magnetic flux at the X line, while the half-width of the current sheet is determined by the half-thickness of J_{ey}, where J_{ey} is the electron out-of-plane current density. From the figure, we can find that magnetic reconnection occurs at about $\Omega_i t = 33$, which is accompanied by the rapid increase of the reconnection electric field. Before that time, we can still observe the excitation of the tearing mode instability with six wavelengths in the current sheet and only one major X line is fully developed (not shown). Magnetic reconnection saturates at about $\Omega_i t = 41$, and at that time the reconnection electric field reaches its peak value, which is about $E_y = 0.22V_AB_0$. We can also find the thinning of the current sheet before the occurrence of magnetic reconnection, and the half-width of the current sheet is about $\delta = 0.18d_i$ or $\delta = 1.8d_e$ at $\Omega_i t = 33$. Therefore, we can know that the trigger of magnetic reconnection occurs when the width of the current sheet is two electron inertial lengths, which has been demonstrated thoroughly in Liu et al. (2020). In this paper, we will focus on the evolution of magnetic reconnection after the onset phase.

Figure 2 describes the evolution of electron and ion outflows at $\Omega_i t = 33$, 35, 40, and 42. Figures 2(a) and (b) present the electron velocity in the x direction (V_{ex}) and the ion velocity in the x direction (V_{ix}), respectively. The magnetic field lines are also plotted in the figure for reference. The enhancement of the electron outflow appears at about $\Omega_i t = 33$, just after the onset phase, which is followed by the rapid increase of the reconnection electric field. At that time, the width of the current sheet is on electron scales. The enhancement of the ion outflow appears at about $\Omega_i t = 40$ when the reconnection electric field is sufficiently large. At $\Omega_i t = 42$, the peak value of the ion outflow speed is about $1.0V_A$, while that of the electron outflow speed can reach about $2.0V_A$. We can also find that the peak of the electron outflow is located much closer to the X line than that of the ion outflow. The electron outflow around the X line is located at the center of the current sheet. After entering the IDR, the electrons become magnetized and leave away from the X line along the magnetic field in the outflow region. We can also find the electron inflow toward the X line along the separatrix regions. This kind of electron flow has also been studied in Lu et al. (2010) and Divin et al. (2012).

The spatial distributions of the electron and ion outflows can be identified more clearly in Figure 3, which plots the profiles of the electron velocity V_{ex} and ion velocity V_{ix} along the line

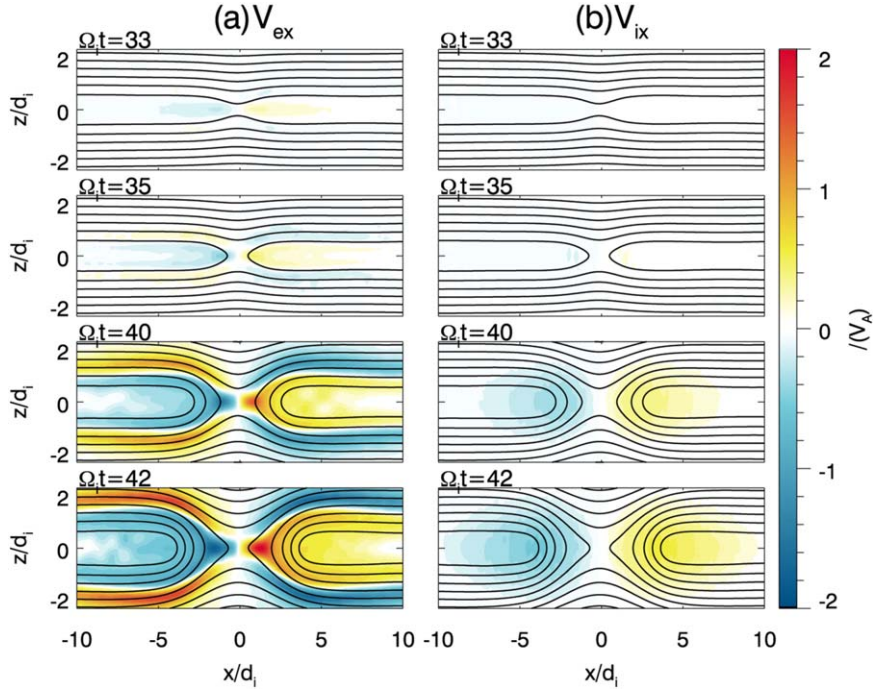

Figure 2. The evolution of (a) the electron bulk velocity $V_{\rm ex}$ and (b) the ion bulk velocity V_{ix} at $\Omega_i t = 33$, 35, 40, and 42, respectively.

$z = 0$ at $\Omega_i t = 33$, 35, 37, and 40. The magnetic field B_z is also plotted for reference. After magnetic reconnection is initiated at $\Omega_i t = 33$, both the reconnection electric field and magnetic field B_z are generated around the X line. The electrons are accelerated around the X line, and an electron outflow is formed when these electrons are away from the X line and deflected by the magnetic field B_z (Lu et al. 2013; Huang et al. 2020). Along the line $z = 0$, the evolution of the magnetic field B_z can be described as

$$\frac{dB_z}{dt} \approx -B_z \frac{\partial V_{\rm ex}}{\partial x}. \tag{3}$$

Equation (3) has been proven in Huang et al. (2015). From the figure, we can easily find that the electron outflow is braked behind the location where the magnetic field B_z reaches its peak, and it will lead to the increase of B_z. The increase of B_z will decelerate the electron outflow more easily. Such a feedback process will lead to the enhancement of B_z. When the magnetic field B_z is sufficiently large, an ion outflow is formed. Obviously, the peak of the electron outflow is closer to the X line than that of the magnetic field B_z, while the peak of the ion outflow is farther away from the X line than that of the magnetic field B_z. Their distances from the X line are about $1.0d_i$, $2.3d_i$, and $2.8d_i$ at $\Omega_i t = 40$, respectively.

Figure 4 shows the distributions of $\boldsymbol{E}\cdot\boldsymbol{J}_e$ and $\boldsymbol{E}\cdot\boldsymbol{J}_i$ at $\Omega_i t = 33$, 37, 40, and 42. Here, $\boldsymbol{E}\cdot\boldsymbol{J}_e$ and $\boldsymbol{E}\cdot\boldsymbol{J}_i$ are the work done by the electric field to electrons and ions, respectively. The positive value of $\boldsymbol{E}\cdot\boldsymbol{J}_e$ is located mainly at the vicinity of the X line, and it means that electrons obtain their bulk velocity after they are accelerated mainly by the reconnection electric field at the vicinity of the X line. Its extent expands over time. At about $\Omega_i t = 37$, a negative value of $\boldsymbol{E}\cdot\boldsymbol{J}_e$ begins to appear behind the location of the peak of B_z. As indicated by the black arrows, the typical negative values of $\boldsymbol{E}\cdot\boldsymbol{J}_e$ are about -0.08 $en_0V_A^2B_0$ and -0.05 $en_0V_A^2B_0$ at $\Omega_i t = 37$, $-0.05en_0V_A^2B_0$, -0.10 $en_0V_A^2B_0$ at $\Omega_i t = 40$, and -0.15 $en_0V_A^2B_0$ and -0.10 $en_0V_A^2B_0$ at $\Omega_i t = 42$, respectively. A negative value of $\boldsymbol{E}\cdot\boldsymbol{J}_e$ means that the electron kinetic energy is transferred into magnetic energy (Karimabadi et al. 2007). This is consistent with the results in Figure 3: around the location with the peak B_z, the electron bulk velocity is braked and magnetic field is enhanced. $\boldsymbol{E}\cdot\boldsymbol{J}_i$ is located ahead of the region with a peak value of the magnetic field B_z, where ions get their bulk velocity.

Because the electron mass and inertia are extremely small, the electron momentum equation can be described as $n_e m_e dV_{\rm ex}/dt = -en_eE_x + (\boldsymbol{J}_e \times \boldsymbol{B})_x - (\nabla\cdot\overleftrightarrow{\boldsymbol{P}_e})_x \approx 0$. Considering that plasma is approximately neutral, $n_e \approx n_i \approx n$. Therefore, the ion momentum equation along $z = 0$ can be written as

$$n_i m_i \frac{dV_{\rm ix}}{dt} \approx J_y B_z - (\nabla\cdot(\overleftrightarrow{\boldsymbol{P}_i} + \overleftrightarrow{\boldsymbol{P}_e}))_x \tag{4}$$

(Huang et al. 2020). Where $J_y = J_{iy} + J_{ey}$, $J_yB_z \approx (\boldsymbol{J}\times\boldsymbol{B})_x$. Figure 5 plots (a) the first, (b) the second, and (c) the sum terms on the right-hand side of Equation (4) along the line $z = 0$ at $\Omega_i t = 33$, 35, 38, and 40, respectively. Obviously, the Lorentz force J_y B_z tends to accelerate ions to form ion outflow. However, during the process of ion acceleration, the term $-(\nabla\cdot(\overleftrightarrow{\boldsymbol{P}_i} + \overleftrightarrow{\boldsymbol{P}_e}))_x$ appears and tries to drag the ion outflow (Huang et al. 2020). Figure 6 shows (a) the current density in the y direction J_y and (b) the magnetic field in the z direction B_z along the line $z = 0$ at $\Omega_i t = 33$, 35, 38, and 40, respectively. We can find that the enhancement of the Lorentz force J_y B_z is caused by the pileup of the magnetic field due to the brake of electron outflow.

3.2. Guide Field Reconnection

To understand the physics behind the transition from electron scales to ion scales in collisionless magnetic reconnection more

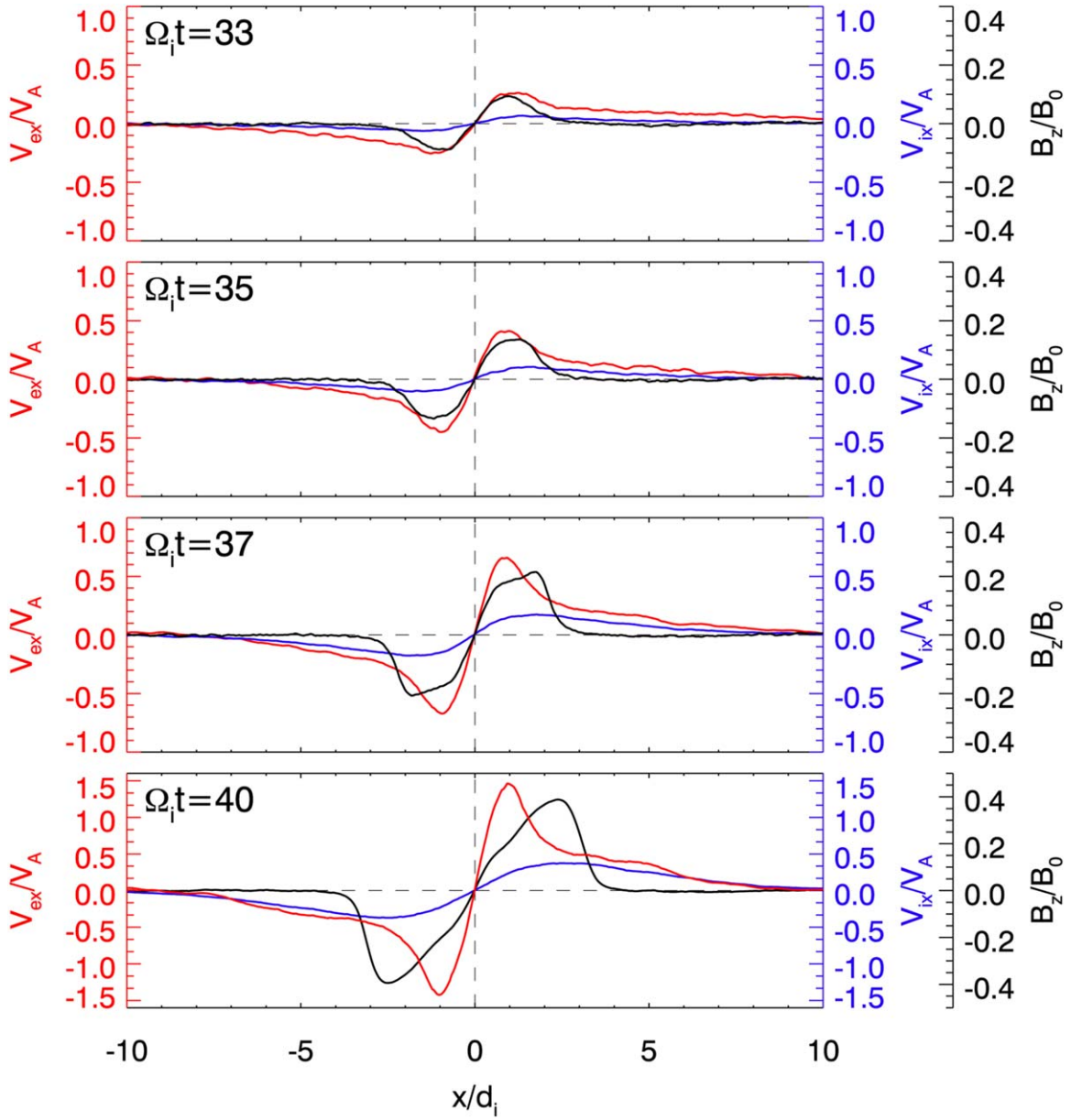

Figure 3. The cuts of electron outflow velocity V_{ex} (red line), ion outflow velocity V_{ix} (blue line), and B_z (black line) along the line $z = 0$ at $\Omega_i t = 33$, 35, 37, and 40, respectively.

clearly, in this section, we will study this evolution process in guide field reconnection.

Figure 7 gives the evolution of the reconnection electric field E_y and the half-width of the current sheet (δ) across the X line in guide field reconnection. Here, reconnection occurs at about $\Omega_i t = 102$ and saturates at $\Omega_i t = 120$, and the reconnection rate is lower than that in antiparallel reconnection. The maximum reconnection electric field is about $E_y = 0.14 V_A B_0$ at $\Omega_i t = 118$. The half-width of the current sheet is approximately $0.15 d_i$ or $1.5 d_e$ at $\Omega_i t = 102$. Similar to antiparallel reconnection, here the evolution of guide field reconnection also begins from electron scales.

The time evolution of the electron and ion outflows at $\Omega_i t = 105$, 110, 115 and 120 is illustrated in Figure 8. Due to the existence of the guide field, both the electron and ion outflows are not directed away from the X line along the center of the current sheet. After the electrons are accelerated in the vicinity of the X line, they leave along the upper left and lower right branches of the separatrices out of the EDR. The ion outflow is formed at about $\Omega_i t = 115$, which is much smaller than the electron outflow. Figure 9 depicts the profiles of the electron and ion outflows along the line $z = 0$ at $\Omega_i t = 102$, 105, 110, and 115. The magnetic field B_z is also plotted for reference. Similar to that in antiparallel reconnection, away from the X line, the electron outflow first reaches its peak, then the magnetic field B_z, and at last the ion outflow. It means that the ions are accelerated mainly in the pileup region.

Figure 10 presents (a) $E_\perp \cdot J_{e\perp}$, (b) $E_{||} J_{e||}$, (c) $\boldsymbol{E} \cdot \boldsymbol{J}_e$, (d) $E_\perp \cdot J_{i\perp}$, (e) $E_{||} J_{i||}$, and (f) $\boldsymbol{E} \cdot \boldsymbol{J}_i$ terms at $\Omega_i t = 115$. The positive value of $\boldsymbol{E} \cdot \boldsymbol{J}_e$ is located mainly at the vicinity of the X line, and electrons obtain their bulk velocity at the vicinity of the X line, while a negative value of $\boldsymbol{E} \cdot \boldsymbol{J}_e$, which is contributed

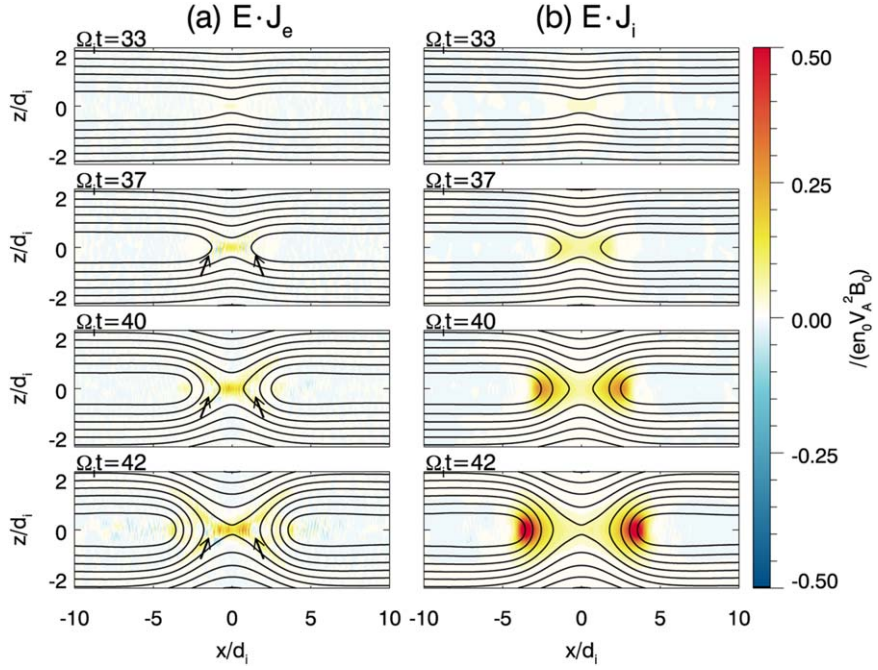

Figure 4. The evolution of the energy conversion, (a) $\boldsymbol{E}\cdot\boldsymbol{J}_e$ term and (b) $\boldsymbol{E}\cdot\boldsymbol{J}_i$ term at $\Omega_i t = 33$, 37, 40, and 42 from the top to the bottom panels, respectively. The black arrows indicate the negative value of $\boldsymbol{E}\cdot\boldsymbol{J}_e$, and the black lines represent the in-plane magnetic field.

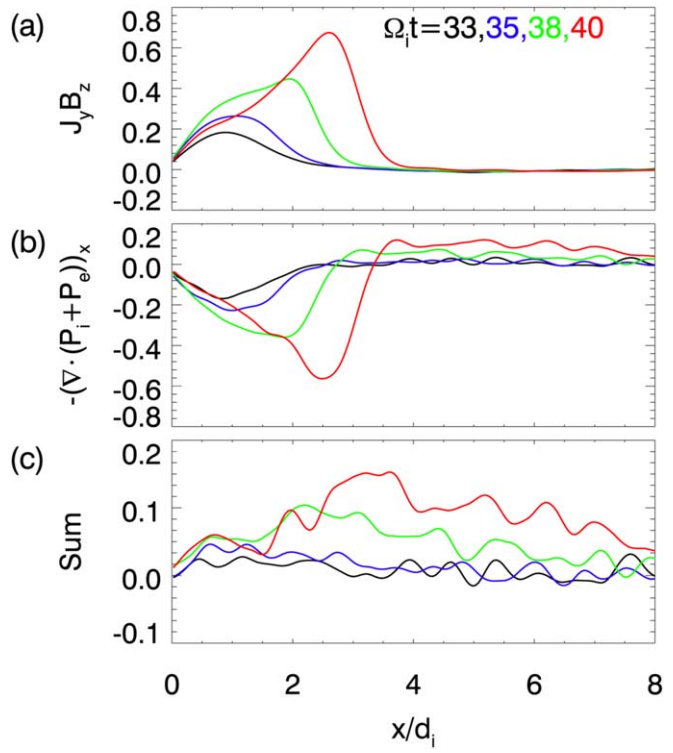

Figure 5. The profiles of forces on ions, (a) the Lorentz force $J_y\,B_z$, (b) the pressure term $-(\nabla\cdot(\overleftrightarrow{\boldsymbol{P}_i}+\overleftrightarrow{\boldsymbol{P}_e}))_x$, and (c) the sum of the Lorentz force and pressure term at $\Omega_i t = 33$, 35, 38, and 40 along $z = 0$ in the positive x direction, respectively.

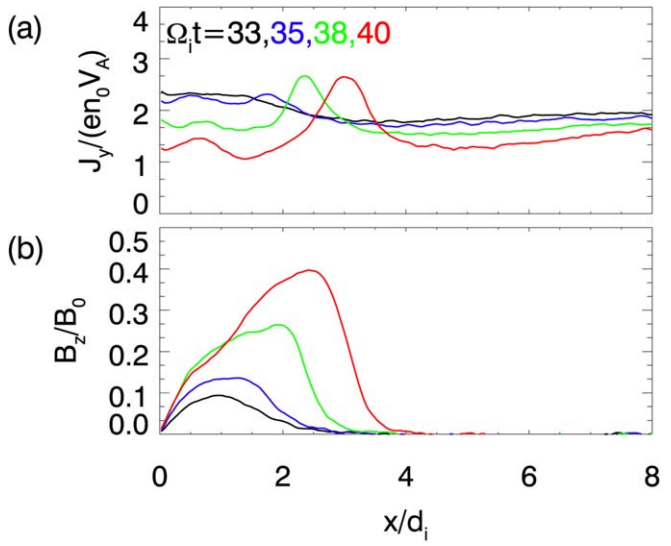

Figure 6. The cuts of (a) out-of-plane current density J_y and (b) magnetic field B_z at $\Omega_i t = 33$, 35, 38, 40 along $z = 0$ in the positive x direction, respectively.

mainly by $E_{||}J_{e||}$, begins to appear before the magnetic field B_z reaches its peak. The positive value of $\boldsymbol{E}\cdot\boldsymbol{J}_i$, which is contributed mainly by $E_\perp\cdot\boldsymbol{J}_{i\perp}$ around the pileup region, is where the ions are accelerated and can obtain their bulk velocity. In antiparallel reconnection, $\boldsymbol{E}\cdot\boldsymbol{J}_e$ and $\boldsymbol{E}\cdot\boldsymbol{J}_i$ are contributed mainly by $E_\perp\cdot\boldsymbol{J}_{e\perp}$ and $E_\perp\cdot\boldsymbol{J}_{i\perp}$, respectively, because $E_{||}$ is negligible.

Here, the ion motions can be described by the following equation:

$$n_i m_i \frac{dV_{\rm ix}}{dt} \approx J_y B_z - B_y J_z - (\nabla\cdot(\overleftrightarrow{\boldsymbol{P}_i}+\overleftrightarrow{\boldsymbol{P}_e}))_x. \quad (5)$$

Figure 11 shows the contour of (a) the Lorentz force $J_y\,B_z$, (b) the Lorentz force $-B_yJ_z$, (c) the pressure term $-(\nabla\cdot(\overleftrightarrow{\boldsymbol{P}_i}+\overleftrightarrow{\boldsymbol{P}_e}))_x$, and (d) the sum of the three forces at $\Omega_i t = 115$. Similar to antiparallel reconnection, the ion outflow is dominated mainly by the $J_y\,B_z$ term.

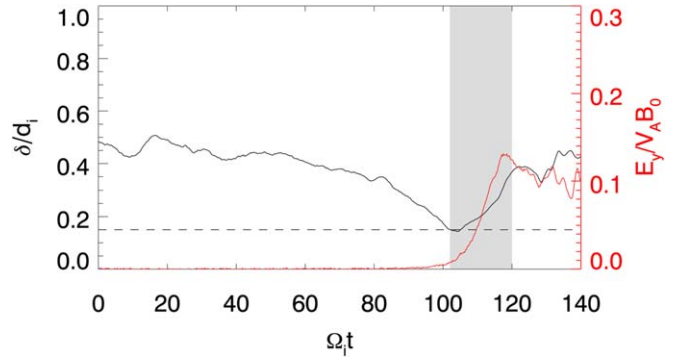

Figure 7. Case with a guide field. The time evolution of the reconnection electric field E_y at X line (red line) and the half-thickness of the electron current sheet δ (black line); the dashed line represents the minimum of the δ (about $0.15d_i$, which is equal to $1.5d_e$). Similar to antiparallel reconnection, we focus on the fast reconnection phase in the gray period from $\Omega_i t = 102$ to $\Omega_i t = 120$.

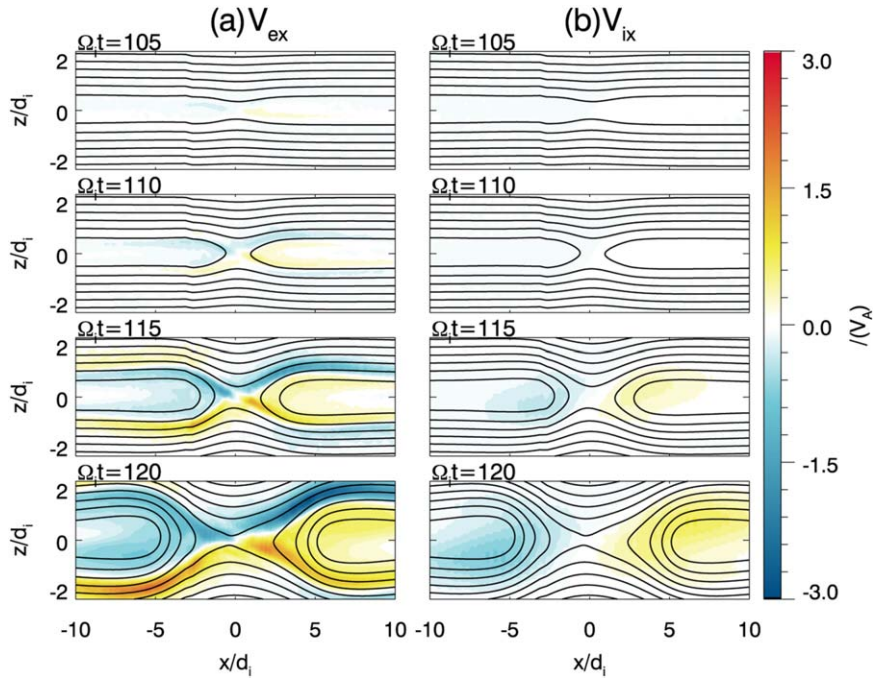

Figure 8. Guide field case. The evolution of outflows in the guide field reconnection, (a) the electron bulk velocity V_{ex} and (b) the ion bulk velocity V_{ix} at $\Omega_i t = 105$, 110, 115, and 120, respectively.

4. Conclusions and Discussion

In this paper, with the help of a 2D PIC simulation model, we study the process of collisionless magnetic reconnection from the onset phase on electron scales to the formation of ion outflow in both antiparallel and guide field reconnection. At first, magnetic reconnection is triggered when the width of the current sheet is thinned to several electron inertial lengths, and both the reconnection electric field and magnetic field B_z are produced during the onset of magnetic reconnection. The electrons are accelerated in the vicinity of the X line by the reconnection electric field and leave away to form a high-speed electron outflow. Then, we can observe the pileup of the magnetic field B_z in the outflow region. When the magnetic field B_z is sufficiently large, the ions are accelerated in the pileup region along the x direction by the Lorentz force, and at last an ion outflow at about one Alfvén speed is formed. In this way, magnetic reconnection is transferred from electron scales to ion scales. The introduction of the guide field will not change the above conclusions, although the symmetry of the electron and ion outflows is distorted. In antiparallel reconnection, both the electron and ion outflows are directed away the X line along the center of the current sheet, while in guide field reconnection the directions of the electron and ion outflows will be deviated from the center of the current sheet.

Therefore, the evolution of magnetic reconnection from electron scales to ion scales has two stages. At the first stage, the Harris current sheet is compressed, and magnetic reconnection is triggered when the width is about several electron inertial lengths. At the second stage, the magnetic field is piled up in the outflow region by the high-speed electron flow from the X line, and then an ion outflow is formed in the pileup region. Liu et al. (2020) focused on the first stage, and found that at that stage the reconnection rate is still too low to convert the upstream magnetic flux to the downstream magnetic flux, which leads to the compression of the current sheet and the onset of magnetic reconnection. In this paper, we investigate the following evolution after the onset of magnetic reconnection, and found that the pileup of the magnetic field B_z

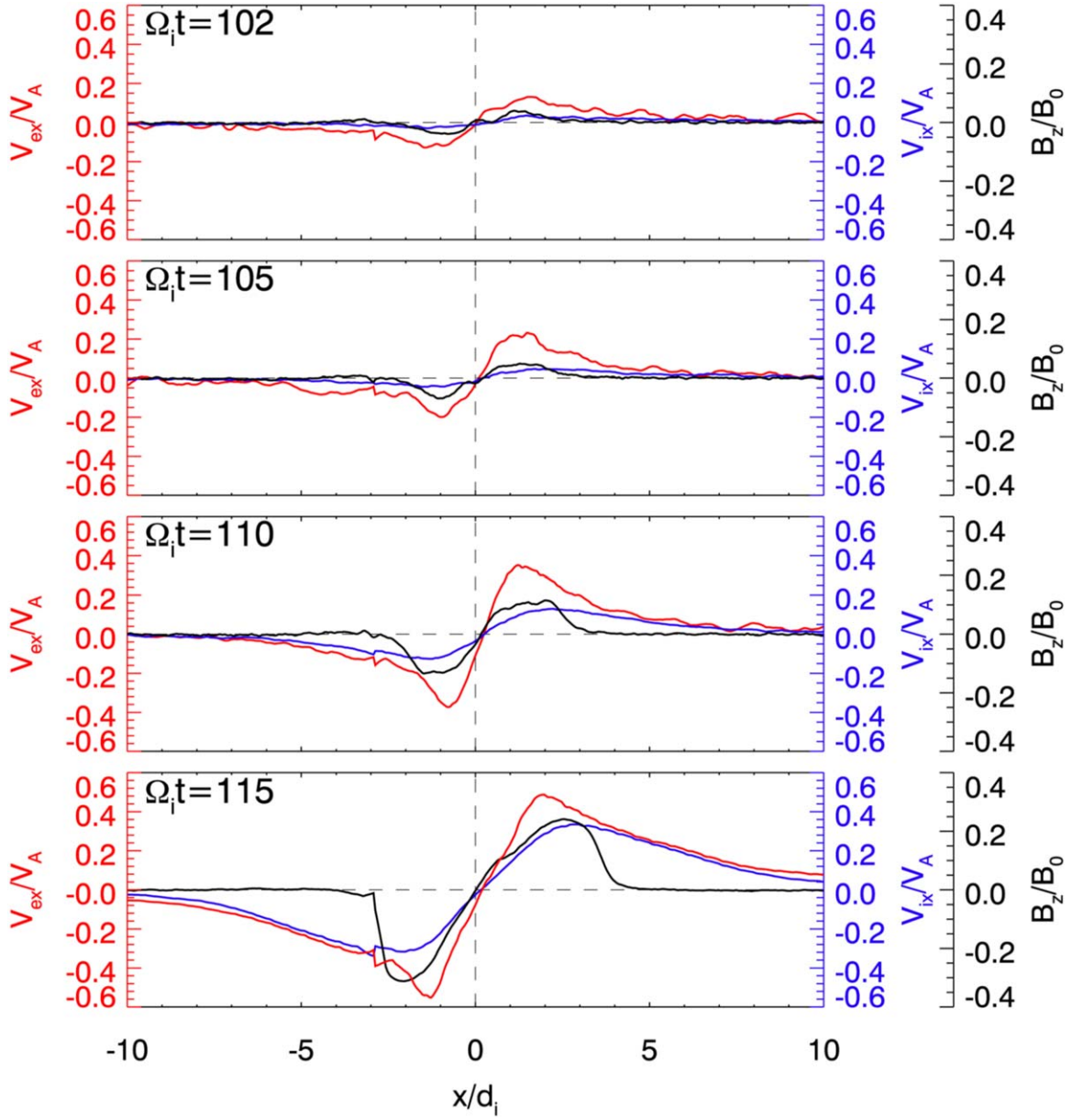

Figure 9. Guide field case. The cuts of electron outflow velocity V_{ex} (red line), ion outflow velocity V_{ix} (blue line), and B_z (black line) along the line $z = 0$ at $\Omega_i t = 102$, 105, 110, and 115, respectively.

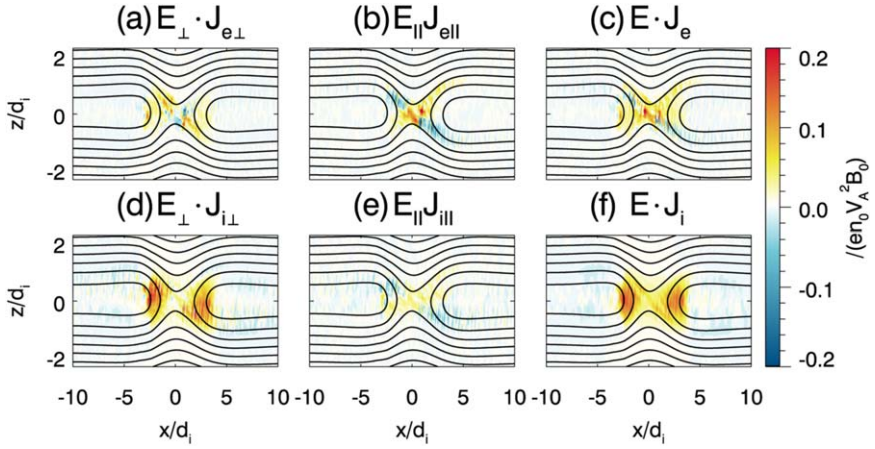

Figure 10. Guide field case. The evolution of the energy conversion in the guide field reconnection. (a) $E_\perp \cdot \boldsymbol{J}_{e\perp}$, (b) $E_{||}\boldsymbol{J}_{e||}$, (c)$\boldsymbol{E} \cdot \boldsymbol{J}_e$, (d) $E_\perp \cdot \boldsymbol{J}_{i\perp}$, (e) $E_{||}\boldsymbol{J}_{i||}$, and (f) $\boldsymbol{E} \cdot \boldsymbol{J}_i$ terms at $\Omega_i t = 115$, respectively.

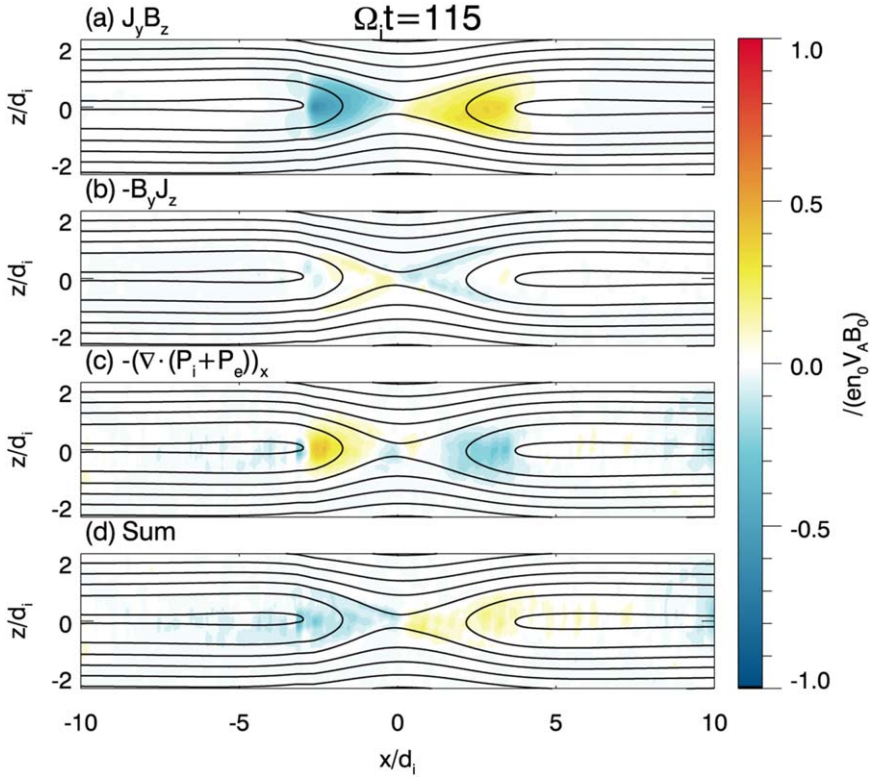

Figure 11. Guide field case. The contour of the forces on ions, (a) the Lorentz force $J_y B_z$, (b) the Lorentz force $-B_yJ_z$, (c) the pressure term $-(\nabla\cdot(\overleftrightarrow{P_i}+\overleftrightarrow{P_e}))_x$, and (d) the sum of the three forces at $\Omega_i t = 115$, respectively.

plays an important role in the transition of collisionless magnetic reconnection from electron scales to ion scales. The pileup of B_z is caused by the deceleration of the electron outflow, and the reason for this deceleration is the existence of B_z. This is a positive feedback process, and mediated by electron kinetics. As described in Lu et al. (2013) and Huang et al. (2020), the generation of the reconnection electric field during the onset of the collisionless magnetic field is also a self-reinforcing process. The growth of E_y is mainly contributed by the electron pressure tensor term, and the electrons are accelerated by the reconnection electric field in the vicinity of the X line, which in turn result in self-reinforcing feedback of E_y.

In reality, collisionless magnetic reconnection is non-stationary. The onset process can be triggered spontaneously or by an external force, and it is not easy to be identified by satellite observations because it occurs on electron scales. Most observed reconnection events by satellites occur on ion scales, and the salient properties include the formation of ion outflow, the quadrupolar structure of the out-of-plane magnetic field, etc. (Nagai et al. 2001; Mozer et al. 2008; Eastwood et al. 2010). Recently, with the high spatial and temporal resolution plasma data provided by NASA's Magnetospheric Multiscale mission, several electron-scale reconnection events are reported (Chen et al. 2016; Phan et al. 2016; Wang et al. 2017; Li et al. 2019; Zhong et al. 2020; Hubbert et al. 2021). This gives us a chance to study the evolution of magnetic reconnection from electron scales to ion scales with satellite observations, and it is our future investigation.

This work was supported by Key Research Program of Frontier Sciences, CAS (QYZDJ-SSW-DQC010), the Strategic Priority Research Program of Chinese Academy of Sciences, Grant No. XDB 41000000, National Science Foundation of China (NSFC) Grants (41774169), and the Fundamental Research Funds for the Central Universities WK2080000164 and WK3420000017.

ORCID iDs

Kai Huang https://orcid.org/0000-0003-3630-309X
Quanming Lu https://orcid.org/0000-0003-3041-2682
San Lu https://orcid.org/0000-0003-2248-5072
Rongsheng Wang https://orcid.org/0000-0002-9511-7660

References

Angelopoulos, V., McFadden, J. P., Larson, D., et al. 2008, Sci, 321, 931
Aunai, N., Belmont, G., & Smets, R. 2011, CRPhy, 12, 141
Bhattacharjee, A., Ma, Z. W., & Wang, X. G. 2001, PhPl, 8, 1829
Birn, J., & Hesse, M. 2009, AnGeo, 27, 1067
Birn, J., & Hesse, M. 2014, JGRA, 119, 290
Biskamp, D. 2000, Magnetic Reconnection in Plasmas (Cambridge: Cambridge Univ. Press)
Chen, L. J., Hesse, M., Wang, S., et al. 2016, GeoRL, 43, 6036
Coppi, B., Laval, G., & Pellat, R. 1966, PhRvL, 16, 1207
Daughton, W., & Karimabadi, H. 2007, PhPl, 14, 072303
Divin, A., Lapenta, G., Markidis, S., Newman, D. L., & Goldman, M. V. 2012, PhPl, 19, 042110
Drake, J. F., & Lee, Y. C. 1977, PhFl, 20, 1341
Drake, J. F., Shay, M. A., Thongthai, W., & Swisdak, M. 2005, PhRvL, 94, 095001
Eastwood, J. P., Shay, M. A., Phan, T. D., & Oieroset, M. 2010, PhRvL, 104, 205001
Forbes, T. G., & Priest, E. R. 1982, P&SS, 30, 1183
Fu, X. R., Lu, Q. M., & Wang, S. 2006, PhPl, 13, 012309
Giovanelli, R. G. 1946, Natur, 158, 81
Harris, E. G. 1962, NCim, 23, 115
Hesse, M., & Schindler, K. 2001, Earth Planets Space, 53, 645

Hesse, M., Schindler, K., Birn, J., & Kuznetsova, M. 1999, PhPl, 6, 1781
Huang, C., Lu, Q. M., Wu, M. Y., Lu, S., & Wang, S. 2013, JGRA, 118, 991
Huang, C., Wu, M. Y., Lu, Q. M., Wang, R. S., & Wang, S. 2015, JGRA, 120, 1759
Huang, K., Huang, C., Dong, Q. L., et al. 2017, PhPl, 24, 041406
Huang, K., Liu, Y. H., Lu, Q. M., & Hesse, M. 2020, GeoRL, 47, e2020GL088147
Huang, K., Lu, Q.-M., Wang, R.-S., & Wang, S. 2020, ChPhB, 29, 075202
Hubbert, M., Qi, Y., Russell, C. T., et al. 2021, GeoRL, 48, e2020GL091364
Ji, H. T., Yamada, M., Hsu, S., & Kulsrud, R. 1998, PhRvL, 80, 3256
Karimabadi, H., Daughton, W., & Scudder, J. 2007, GeoRL, 34, L13104
Karimabadi, H., Huba, J. D., Krauss-Varban, D., & Omidi, N. 2004, GeoRL, 31, L07806
Li, X. M., Wang, R. S., Lu, Q. M., et al. 2019, GeoRL, 46, 14263
Liu, D. K., Lu, S., Lu, Q. M., Ding, W. X., & Wang, S. 2020, ApJL, 890, L15
Liu, Y. H., Birn, J., Daughton, W., Hesse, M., & Schindler, K. 2014, JGRA, 119, 9773
Liu, Y. H., Hesse, M., Guo, F., et al. 2017, PhRvL, 118, 085101
Lu, Q. M., Huang, C., Xie, J. L., et al. 2010, JGRA, 115, A11208
Lu, Q. M., Lu, S., Huang, C., Wu, M. Y., & Wang, S. 2013, PPCF, 55, 085019
Lu, Q. M., Wang, H. Y., Wang, X. Y., et al. 2020, GeoRL, 47, e2019GL085661
Lu, S., Wang, R., Lu, Q., et al. 2020, NatCo, 11, 5049
Mozer, F. S., Angelopoulos, V., Bonnell, J., Glassmeier, K. H., & McFadden, J. P. 2008, GeoRL, 35, L17S04
Nagai, T., Shinohara, I., Fujimoto, M., et al. 2001, JGRA, 106, 25929
Parker, E. N. 1957, JGR, 62, 509
Pei, W. B., Horiuchi, R., & Sato, T. 2001, PhRvL, 87, 235003
Phan, T. D., Eastwood, J. P., Cassak, P. A., et al. 2016, GeoRL, 43, 6060
Pritchett, P. L. 2001, JGRA, 106, 3783
Pu, Z. Y., Chu, X. N., Cao, X., et al. 2010, JGRA, 115, A02212
Ren, Y., Yamada, M., Gerhardt, S., et al. 2005, PhRvL, 95, 055003
Sang, L. L., Lu, Q. M., Wang, R. S., Huang, K., & Wang, S. 2019, ApJ, 877, 155
Schindler, K. 1991, GApFD, 62, 37
Shay, M. A., Drake, J. F., Denton, R. E., & Biskamp, D. 1998, JGRA, 103, 9165
Shay, M. A., Drake, J. F., Rogers, B. N., & Denton, R. E. 1999, GeoRL, 26, 2163
Shay, M. A., Drake, J. F., & Swisdak, M. 2007, PhRvL, 99, 155002
Speiser, T. W. 1965, JGR, 70, 4219
Sweet, P. A. 1958, The Neutral Point Theory of Solar Flares, 6, 123
Vasyliunas, V. M. 1974, Eos T Am Geophys Un, 55, 975
Wan, W. G., & Lapenta, G. 2008, PhPl, 15, 102302
Wang, R. S., Nakamura, R., Lu, Q. M., et al. 2017, PhRvL, 118, 175101
Wang, S., & Lu, Q. M. 2019, Collisionless Magnetic Reconnection (Beijing: Science Press)
Wang, X. G., Bhattacharjee, A., & Ma, Z. W. 2000, JGRA, 105, 27633
Yamada, M. 1999, JGRA, 104, 14529
Zhong, Z. H., Zhou, M., Tang, R. X., et al. 2020, ApJL, 892, L5
Zhou, F. S., Huang, C., Lu, Q. M., Xie, J. L., & Wang, S. 2015, PhPl, 22, 092110